The application of a radar-based depth inversion method to monitor near-shore nourishments on an open sandy coast and an ebb-tidal delta

Gawehn, Matthijs; van Dongeren, Ap; de Vries, Sierd; Swinkels, Cilia; Hoekstra, Roderik; Aarninkhof, Stefan; Friedman, Joshua

DOI
10.1016/j.coastaleng.2020.103716

Publication date
2020

Document Version
Accepted author manuscript

Published in
Coastal Engineering

Title: The application of a radar-based depth inversion method to monitor near-shore nourishments on an open sandy coast and an ebb-tidal delta

Authors: Matthijs Gawehn[1,3], Ap van Dongeren[1] , Sierd de Vries[3], Cilia Swinkels[2], Roderik Hoekstra[2], Stefan Aarninkhof[3], Joshua Friedman[2]

[1]Department of Applied Morphodynamics, Unit of Marine and Coastal Systems, Deltares, Delft, Netherlands, [2]Department of Harbours Coasts and Offshore, Unit of Hydraulic Engineering, Deltares, Delft, Netherlands, [3]Faculty of Civil Engineering and Geosciences, Delft University of Technology, Delft, Netherlands

Corresponding author: M. A. Gawehn; Matthijs.Gawehn@deltares.nl, m.a.gawehn@tudelft.nl

Keywords:

- Remote sensing
- Depth inversion
- X-Band radar
- Tidal inlet
- Coastal Zone
- Nourishment

Abstract

Coastal management in the Netherlands has the aim to defend coastal zones by preventing flooding and mitigating erosion. To that end, large-scale nourishments are placed in the nearshore, which are supposed to dynamically preserve the coastal zone over a timescale of years. To assess their effectiveness, these nourishments are monitored over large areas and long durations. As repetitive, in-situ measurements become too expensive, remote sensing offers an attractive alternative, mapping depth and near-surface current fields via depth inversion algorithms (DIA). However, the information that can be derived from remotely-sensed data is subject to improvement. In this study a 3D-FFT based DIA named XMFit (**X**-Band **M**atlab **Fit**ting) is introduced, which is robust, accurate and fast enough for operational use. Focusing on depth estimates, the algorithm was validated for two case studies in the Netherlands: (1) the "Sand Engine", a beach mega nourishment at a uniform open coast, and (2) the tidal inlet of the Dutch Wadden Sea island Ameland, characterizing a more complex coast. Considering both sites, the algorithm performance was characterized by a spatially averaged depth bias of -0.9 m at the Sand Engine and a time-varying bias of approximately -2 – 0 m at the Ameland Inlet. When compared to in-situ depth surveys the accuracy was lower, but the time resolution higher. Depth estimates from the Ameland tidal inlet were produced every 50 min by an operational system using a navigational X-Band radar to monitor the placement of a 5 million m^3 ebb-tidal delta nourishment – a pilot measure for coastal management. Volumetric changes in the nourishment area over the year 2018, occurring at 7 km distance from the radar, were estimated with an error of 7%. Depth errors statistically correlated with the direction and magnitude of simultaneous near-surface current estimates. Additional experiments on Sand Engine data demonstrated that depth errors may be significantly reduced using an alternative spectral approach and/or by using a Kalman filter.

1 Introduction

With the extensive urbanization of the coastal hinterland, the role of coastal management in the Netherlands has become increasingly important to ensure flood safety and the protection of recreational and ecological values of the coast. Modern coastal maintenance strives towards a “building with nature” approach (de Vriend and van Koningsveld, 2012), using soft engineering strategies to mitigate long-term coastal recession. Along uniform coastlines, large 1-2 million m^3 shoreface nourishments have proved to be an effective strategy (Hamm et al., 2002), and a basic understanding has been established about their behaviour (Huisman et al., 2019; Lodder and Sørensen, 2015). In pursuit of finding the optimal long-term solution, larger nourishment designs have been explored of which the Sand Engine, a beach mega-nourishment comprising 21 million m^3 of sand is a famous example (Stive et al., 2013). In the meantime even bigger nourishments have been placed with volumes up to 36 million m^3 (Kroon et al., 2016). The most recent experiment involved the construction of a 5 million m^3 nourishment in the outer delta of a complex tidal inlet system at the Wadden Sea island Ameland.

To evaluate the success of these innovative coastal management interventions it is necessary to map them and to monitor their evolution. Due to the large nourishment volumes and long lifetime, monitoring with in-situ techniques is expensive and it may be favorable to use remote sensing techniques instead. Such techniques can capture morphological variability at a large spatial scale in high temporal resolution over long periods of time (Bergsma et al., 2019). To be used in an operational setting, remote sensing techniques need to be robust. We define robust as being able to handle variations in environmental conditions and data quality without the need for manual adjustments and costly person hours. Here, we propose to derive bathymetries with a technique that meets these desired requirements and uses already available X-Band radar data from a lighthouse.

Marine radars operating in the X-Band range are routinely deployed aboard ships and on marine traffic control towers to detect vessels and other floating objects. In coastal areas, such radars may also be used to monitor waves, currents and water depths. Their benefits over in-situ depth surveys are a high spatial and temporal coverage and lower operating and maintenance costs. However, the spatial resolution of X-Band radars can be coarse and, as sampling frequencies are often low, they have a lacking ability to recognize shorter period waves. Moreover, an inherent uncertainty exists in relating radar image intensities to the observed ocean surface properties, bringing challenges to the analysis of X-Band radar data. Moreover, X-Band radars are expensive instruments, which is why it may be attractive to exploit existing navigational radars in areas of interest.

Although considered “noise” for navigational purposes, the wave field leaves a signature on an X-Band radar known as sea clutter. This imprint is produced by radar signal reflection off capillary waves, which are modulated by the underlying surface gravity wave field (Borge et al., 2004; Valenzuela, 1978), the so-called Bragg-scattering (Plant, 1990). Observing the propagation of a wavefield through time offers a possibility to infer information about the waves themselves, but also about currents and depths these waves feel.

In particular for the purpose of depth estimation, several depth inversion algorithms (DIAs) have been developed. Most DIAs use wavefield recordings from either radars or beach cameras, but these methods may be used interchangeably between instruments (Honegger et al., 2019). While some DIAs use a sequence of images (i.e. a video of typically 6-12 min) to link wavenumbers to wave frequencies and estimate depths via the linear dispersion relationship (Bell, 1999; Dugan et al., 2001; Hessner et al., 1999; Holman et al., 2013), other DIAs use the average of a sequence of images (i.e. a time exposure) to estimate depths through spatial patterns of breaking intensity (Aarninkhof et al., 2005; van Dongeren et al., 2008). If the area of interest is large, X-Band radars have an advantage above cameras because of their larger field of view. Other advantages are their operability at night and a smaller sensitvity to rain or sun glare. A large field of view means that depths are estimated far beyond the breaker zone, therefore a dispersion-based DIA is preferred with a sequence of images as input.

The commonly used dispersion-based DIAs to analyse image sequences from XBand-radar, employ three dimensional Fast Fourier Transforms (3D-FFTs) to acquire the necessary wavenumber – frequency relationships. Spatial variations are captured by discretising an image sequence into smaller domains known as computational cubes (x,y,t) (Trizna, 2001). These computational cubes are processed separately. A 3D-FFT then converts each computational cube from the space-time domain (x,y,t) into wave components in the wave number – frequency domain (k_x,k_y,ω). This information is used to constrain the Doppler-shifted linear dispersion shell

$$\omega = \sqrt{g|\boldsymbol{k}|\tanh(|\boldsymbol{k}|d)} + \boldsymbol{U}\cdot\boldsymbol{k} \qquad 1)$$

to estimate the water depth, d (m), and the two horizontal current vector components [u, v] of $\boldsymbol{U}$ (m/s). The gravitational acceleration is given by g, the wave number vector by $\boldsymbol{k}$ (rad/m) with components [k_x, k_y], and ω (rad/s) is the corresponding frequency. The idea to use 3D-FFTs originally came from the estimation of $\boldsymbol{U}$ under known d (Young et al., 1985), however, it could naturally be extended to estimate d as well by keeping d as a free parameter (e.g. Bell, 2008; Hessner et al., 2014; Ludeno et al., 2015; Rutten et al., 2017). The derivation of the Doppler-shift in the form $+\boldsymbol{U}\cdot\boldsymbol{k}$ in equation 1, assumes a depth uniform current equal to $\boldsymbol{U}$. In practice, the current profile is not uniform over depth and the vector $\boldsymbol{U}$ represents a weighted average of velocities in the upper layer of the water column (e.g., assuming a linearly sheared current profile, waves with periods of T = 5-8 s travelling in water depths of d = 5-15 m feel velocities that occur at 20-45% of the water depth; see eq. 5 in Campana et al., 2016). Therefore, $\boldsymbol{U}$ is commonly also referred to as near-surface current (Young et al., 1985; Senet et al., 2001).

Several authors have applied the dispersion relation without Doppler-shift ($+\boldsymbol{U}\cdot\boldsymbol{k}$ in equation 1), neglecting the presence of near-surface currents, to remotely sense d from X-Band radar data (Bell, 1999; Hessner et al., 1999). Although conceptually proven, these early developments were applied to limited datasets and lacked quantitative validation. Later, based on two single daily-averaged estimates from Egmond aan Zee (NL) and Teignmouth Pier (UK), Bell (2001) demonstrated that error margins could be within 1 m accuracy for depths up to 12 m, with exception of the breaker zone where errors were approximately 2 m. For the site of Duck (North Carolina, US) with depths up to 6 m, Trizna (2001) reported depth errors of 0 to 4 m depending on the wave-height and suggested that the inclusion of non-linear wave theory improves estimates. This was then disproven by Flampouris et al. (2011) who, for a site near the Wadden Sea island Sylt (GE), reported root-mean-square-errors (RMSE) of at least 1.6 m regardless of the (non-)linear wave theory used.

For airborne optical video, Dugan et al. (2001) were one of the first to include the Doppler-shift in equation 1, for the joint estimation of d and $\boldsymbol{U}$ using 3D-FFTs. The extension was subsequently also used in the analysis of X-Band radar data from the Dee Estuary (UK) (Bell, 2008). Although near-surface currents could not be validated, it was noted that their inclusion had improved depth estimates, which is consistent with a recent study showing that currents can influence depth estimates significantly (Honegger et al., 2020). Based on three high tide estimates, Bell (2008) found depth errors to be mostly within a 1 m range in the spatial domain, however, estimates in the deep channel (> 20 m) were larger as waves only weakly felt the bottom. More recently, 3D-FFT based DIAs have been applied to complex nearshore situations, for example by Hessner et al. (2014), who built on work done by Seemann et al.

(1997) and Senet et al. (2001) by solving for *d* in addition to ***U*** for an analysis of two days of radar data from a coastal site in New Zealand with strong tidal currents. Their near-surface current estimates reasonably agreed with model data, yet simultaneous depth estimates lacked validation. Similarly, Hessner et al. (2015) investigated a site at the southeast coast of the UK. Here, accumulated depth estimates were compared to ground truth measurements and agreed qualitatively but error metrics were not quantified. Ludeno et al. (2015) used an algorithm proposed by Serafino et al. (2010) to jointly estimate *d* and ***U*** from 45 min of radar data from a ferry near the harbour of Salerno (IT) and used a spatial partitioning technique to accelerate computations. The local depth was between 10 and 20 m, which Ludeno et al. (2015) estimated to have a bias of approximately 1 m. Rutten et al. (2017) were one of the first to explore the possibility of estimating volume budgets from estimates of *d* in the nearshore region over a long time period of one year, taking a first step from research to a potential use of radar based DIAs in coastal management. A large depth bias of 2.3 m for depths smaller than 6 m, however, caused volume estimates to be 3.9 million m^3 short of what was expected. While near-surface current estimates were not presented, they noted that poor *d* estimates concurred with poor ***U*** estimates.

So far, 3D-FFT based depth inversion from XBand-radar data has focussed on the development and (often conceptual) testing of DIAs (Bell, 2008; Hessner et al., 2014; Ludeno et al., 2015). The accuracy of depth estimates is generally in a 1-2 m range and depends on the location, radar, and the algorithm used. Moreover, presented error statistics are mostly based on short, experimental data sets. The accuracy is generally lower in deeper areas where waves are hardly affected by the depth (Bell, 2008) and in very shallow water where waves become non-linear (e.g., Trizna, 2001; Holland, 2001). Even though the validation of near-surface currents themselves is often lacking, it has been reported that including their effect on waves is important: while it improves depth estimates (Bell, 2008), a poor current estimate can also be an indicator for a poor, joint depth estimate (Rutten et al., 2017). The effect of higher significant wave heights, H_s, has been shown to increase depth errors in shallower waters (Trizna, 2001), while a minimum $H_s > 1$ m is needed for sufficient sea-clutter (Bell, 2008).

3D-FFT based DIAs have mostly been applied in an experimental setting and the question arises whether they are ready to be used for practical coastal management purposes, such as the quantification of volumetric changes caused by nourishments. To that end, they need to run operationally on long-term radar data and hence be able to handle variations in environmental conditions and data quality. In this paper, we present a 3D-FFT-based DIA named XMFit (**X**-Band **M**atlab **Fit**ting), which manages such variations by selecting the best values from a set of [d, $\boldsymbol{U}$]-solutions, for every location in the radar domain at any point in time. The generation of a set of solutions is done by a set of different energy thresholds to separate spectral wave data from the noise floor. This is different from other currently used DIAs, which may (i) optimize a [d, $\boldsymbol{U}$]-solution by iterating on a first, high energy threshold guess with a lower energy threshold guess including aliases and higher order effects (Hessner et al., 2014; Senet et al., 2001) or (ii) by maximizing a normalized scalar product between the image amplitude spectrum and a characteristic function, which omits the use of thresholds (Ludeno et al., 2015; Serafino et al., 2010). Similar to those algorithms, the present method also includes the Doppler-shift (equation 1) to allow for the effect of near-surface currents on the depth estimates. XMFit uses different spectral filters, an anti-aliasing step and a least-squares fitting procedure.

We validate the DIA using two different sites in the Netherlands: The Sand Engine, and the ebb-tidal delta of the Ameland Inlet to the Wadden Sea. Detailed ground truth data from 2014 and 2018 are respectively used for validation. With 7.5 km, the XBand-radar range at the Ameland Inlet is double the range previously reported for depth inversion studies and enables us to capture the extensive size of the Inlet. By that, we track a 5 million m^3 ebb-tidal delta nourishment at 7 km distance from the radar, creating a one-year time evolution of its volume.

Section 2 introduces the XMFit algorithm and its features. In section 3, the field sites and data collection are described. Results on validation and monitoring the placement of the nourishment are presented in section 4. In the Discussion section 5, we elaborate on errors and methods to mitigate them and then conclude our findings in section 6. Radar specifics and details on computational settings are documented in the Appendices.

2 Depth-inversion Method

The depth-inversion algorithm XMFit is based on an original idea by Young et al. (1985), where radar image sequences of a wave field are first split into smaller cubes, then processed via 3D-FFT to retrieve spectral wave characteristics, after which the Doppler-shifted dispersion relation can be used to obtain estimates of depth and near-surface currents (equation 1). In order to process an image sequence, the algorithm requires information about the radar, user settings and optionally a bathymetry and a water level (Figure 1, top row). The radar information includes the coordinates of the radar, its radius and the framerate of the image sequence and pixel size. User settings include a grid definition, which consists of the location and size of the computational cubes, and limiters that are used to constrain the analysis.

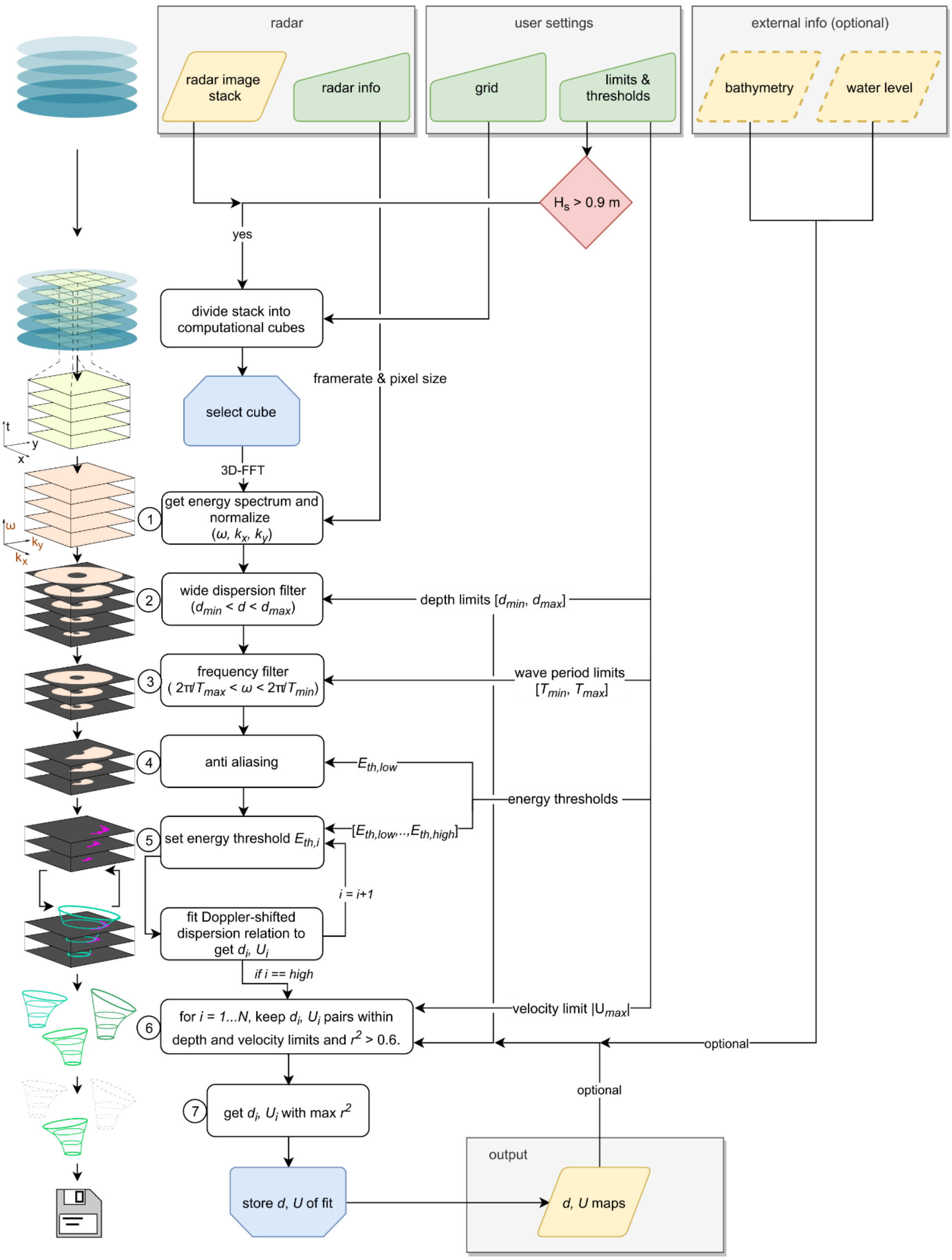

Figure 1. XMFit workflow for depth and near-surface current inversion from an image sequence. Consecutive processing steps in the flowchart are visualized along their left. The flowchart includes: data (brown), user input (green), decision (red), process loop start (blue;

trimmed top corners) and process loop end (blue; trimmed bottom corners), and process (white). Arrows and their annotations signify flow of information. The algorithm requires input on radar specifics, user settings and optionally a bathymetry and water level (grey squares top row). The output contains maps of depth estimates and near-surface current fields (grey square bottom row). Symbols represent: [k_x, k_y] = wavenumber components, ω = wave frequency, [d_{min}, d_{max}] = depth limits, [T_{min}, T_{max}] = wave period limits, |U_{max}| = velocity magnitude limit, [$E_{th,low}$,..$E_{th,i}$,..$E_{th,high}$] = array of spectral energy thresholds, [$d_{,i}$, $U_{,i}$] = depth and near-surface current estimates corresponding to $E_{th,i}$, and [d, U] = optimal depth and near-surface current pair.

Before an image sequence is analysed, a high-pass threshold on the significant wave heights of H_s = 0.9 m is made, similar to (Bell, 2008) as a proxy for sufficient sea-clutter (Figure 1, red diamond). Note that the wave height information has to be provided as an external input to the DIA.

The processing of an image sequence commences by dividing it into a number of computational cubes ($c = 1...N$) according to the user defined grid. Cubes are processed consecutively, each providing an estimate for a depth, d_c, and near-surface current vector, $\boldsymbol{U}_c$, at its location. The inversion of [d_c, $\boldsymbol{U}_c$] consists of seven steps (Figure 1, labels 1..7). Since the procedure is identical for all cubes, we drop the subscript c from here onwards and use [d, $\boldsymbol{U}$] for notational simplicity. The first step is to taper the computational cube with a 3D-Hanning window and to generate a k_x,k_y,ω-energy spectrum via 3D-FFT. If the time-sequence is long enough, the spectrum may also be smoothed through spectral averaging in time, by dividing the cube into smaller time-bins. Using min-max normalization, the spectral energy is then converted to the range [0,1] to prepare it for a fitting procedure later in the process (Figure 1, 1). At this stage, the spectrum carries redundant information in non-relevant spectral components, such as noise and aliases, which can be discarded to save computer memory. A wide-dispersion filter removes spectral energy beyond realistic depths (Figure 1, 2), by means of limiting dispersion shells corresponding to a minimum depth d_{min}, and a maximum depth d_{max}. These limiting dispersion shells do not include a Doppler-shift, as experience shows that it does not provide additional result accuracy but does increase computation time. A frequency filter removes spectral energy beyond realistic wave periods (Figure 1, 3), by means of a minimum wave period T_{min} and a maximum wave period T_{max}. The limits for realistic water depths and wave periods are supplied by the user and are typically set around [d_{min}, d_{max}] = [0.5, 25] (m) and [T_{min}, T_{max}] = [4, 15] (s) respectively; indicating the ranges where we expect waves to be mostly in intermediate or shallow water to get reliable depth estimates. Note that for depths larger than approximately 15 m, shorter period waves ($T < 6$ s) are mainly useful in determining near-surface currents.

If the frame rate of the image sequence is low due to a slow turning radar antenna, as is the case in this study with 1/2.85 s^{-1}, the filtered spectrum may show aliasing since the Nyquist frequency is close to the governing wave periods. An anti-aliasing step removes these unwanted by-products, (Figure 2; Figure 1, 4) and permits the use of data up to two times the Nyquist frequency (Seemann et al., 1997).

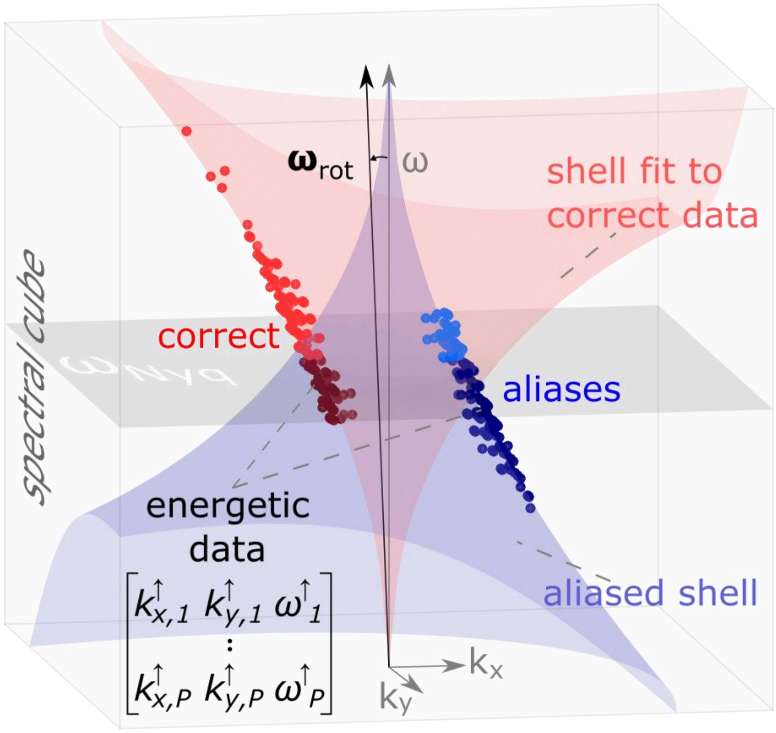

Figure 2. Anti-aliasing on a spectral cube with dimensions k_x, k_y, ω. Energetic spectral data with energies above a threshold $E_{th,low}$ are given by a set of $p = 1 \ldots P$ points with coordinates $k^{\uparrow}_{x,p}$, $k^{\uparrow}_{y,p}$, $\omega^{\uparrow}_{p}$. This set contains correct data points (red dots) and aliases (blue dots), below and above the Nyquist frequency (grey plane). Aliases are detected and removed via a singular value decomposition. The ω-axis rotates ($\boldsymbol{\omega}_{\mathrm{rot}}$) towards the correct spectral data by which aliases can be separated and a non-linear fit can be done on the correct spectral data (red dispersion shell) according to equation 1. The blue shell indicates the orientation of aliases in the spectrum.

To separate the aliases from correct wave data a singular value decomposition (svd) (equation 2) is performed on the energetic parts of the spectrum. Energetic parts are defined by all spectral data with energies above a user defined threshold $E_{th,low}$, which is the lower bound of the set $0 < \{E_{th,low} \ldots E_{th,high}\} < 1$ used in the fitting procedure that follows this anti-aliasing step.

$$\boldsymbol{A} = \boldsymbol{U}\,\boldsymbol{\Sigma}\,\boldsymbol{V}^{\boldsymbol{T}}\,,$$

$$where$$

$$\boldsymbol{A} = \begin{bmatrix} \boldsymbol{k}_x^{\uparrow} & \boldsymbol{k}_y^{\uparrow} & \boldsymbol{\omega}^{\uparrow} \end{bmatrix} = \begin{bmatrix} k_{x,1}^{\uparrow} & k_{y,1}^{\uparrow} & \omega_1^{\uparrow} \\ k_{x,2}^{\uparrow} & k_{y,2}^{\uparrow} & \omega_2^{\uparrow} \\ \vdots & \vdots & \vdots \\ k_{x,P}^{\uparrow} & k_{y,P}^{\uparrow} & \omega_P^{\uparrow} \end{bmatrix} \qquad 2)$$

The matrix $\boldsymbol{A}$ lists the $p = 1\ldots P$ energetic points in the spectrum by their spectral coordinates $k^{\uparrow}_{x,p}$, $k^{\uparrow}_{y,p}$, $\omega^{\uparrow}_{p}$ in the columns $[\boldsymbol{k}^{\uparrow}_{x}, \boldsymbol{k}^{\uparrow}_{y}, \boldsymbol{\omega}^{\uparrow}]$, where the upward arrow signifies energy higher than $E_{th,low}$. The amount of points, P, depends on the value of $E_{th,low}$ and the spectral wave signal. The svd factorizes the matrix $\boldsymbol{A}$ into two unitary matrices $\boldsymbol{U}$, $\boldsymbol{V}$ and a diagonal matrix $\boldsymbol{\Sigma}$. The superscript T denotes the transpose. In practice, $\boldsymbol{V}$ represents a rotation of the k_x,k_y,ω-coordinate system: $\boldsymbol{V} = [\boldsymbol{k}_{x,rot}, \boldsymbol{k}_{y,\mathrm{rot}}, \boldsymbol{\omega}_{\mathrm{rot}}]$, which best follows the spectral data $\boldsymbol{A}$. Due to the position of the aliases in the spectrum, the ω-axis rotates ($\boldsymbol{\omega}_{\mathrm{rot}}$) towards the correct spectral data and away from the aliases, which allows for a clear separation: Correct data have higher values on $\boldsymbol{\omega}_{\mathrm{rot}}$ (found via $\boldsymbol{A}\boldsymbol{\omega}_{\mathrm{rot}}$) compared to the original ω-axis and for aliases this is the opposite, which means that they are identified and can be removed.

After pre-processing the spectrum several spectral fits are done. Using a Levenberg-Marquardt minimisation, the Doppler-shifted linear dispersion relationship (equation 1) is fitted to all spectral data above a certain energy threshold E_{th} to yield an estimate for $[d, \boldsymbol{U}]$. Since the spectrum has been normalized this threshold lies between $0 < E_{th} < 1$. However, the optimal value of E_{th} is not known beforehand. The solution is to iterate an optimal value by making several fits for an array of energy thresholds $\{E_{th,low},\ldots, E_{th,high}\}$, which produces a set of depth and near-surface current pairs $\{[d_{low}, \boldsymbol{U}_{low}],\ldots,[d_{high}, \boldsymbol{U}_{high}]\}$ (Figure 1, 5). By default, $\{E_{th,low},\ldots, E_{th,high}\}$ covers the range $\{0.4, \ldots,0.6\}$ in 10 increments, which is a generic setting, but can be adjusted by the user. By using a set of E_{th}, instead of single threshold, we omit the need to tailor the algorithm to each image sequence separately, which makes the algorithm robust to use on long time-series of data.

The goal is now to find the optimal pair of $[d_i, \boldsymbol{U}_i]$ among the list of candidates $\{[d_{low}, \boldsymbol{U}_{low}],\ldots,[d_{high}, \boldsymbol{U}_{high}]\}$. Pairs are retained using three criteria: (1) d_i falls within the pre-set depth range $[d_{min}, d_{max}]$, (2) $|\boldsymbol{U}_i|$ is smaller than a user-defined maximum velocity magnitude $|\boldsymbol{U}_{max}|$, and (3) the coefficient of determination $r^2 > 0.6$, (Figure 1, ⑥). Note that the depth constraint $[d_{min}, d_{max}]$ has been used in an earlier step to reduce the spectrum with a wide dispersion filter (Figure 1, ②). However, a poor candidate fit on those data may still suggest a solution beyond those limits, therefore criterion (1) is needed here. To improve estimates of an operational system, knowledge about previous depth estimates can be used to (A) tighten criterion (1) or (B) in a Kalman filter. In case of option (A), an average is taken over a certain number of M previous depth estimates, $d_{avg,M}$, and a margin Δd is chosen to tighten criterion (1) by redefining $d_{min,} = d_{avg,M} - ½\Delta d$ and $d_{max} = d_{avg,M} + ½\Delta d$. Option (B) is a postprocessing step and does not affect the depth inversion procedure. In this study we used option (A) for the site of Ameland (section 4) and experimented with option (B) for the Sand Engine (section 5).

The r^2 of criterion (3) is used as the optimization criterion as it indicates how well the non-linear fit represents the spectral data. This value is unity for a perfect match. Hence, the optimal $[d, \boldsymbol{U}]$ amongst the remaining candidates is finally found by the fit with maximum r^2, (Figure 1, ⑦) and can be stored as the representative estimate for the computational cube. After a computational cube has been processed, the sequence of steps repeats for the next computational cube in the grid (Figure 1: steps ①..⑦), eventually producing full maps of depths and near-surface currents (Figure 1, output).

3 Radar in-situ data collection

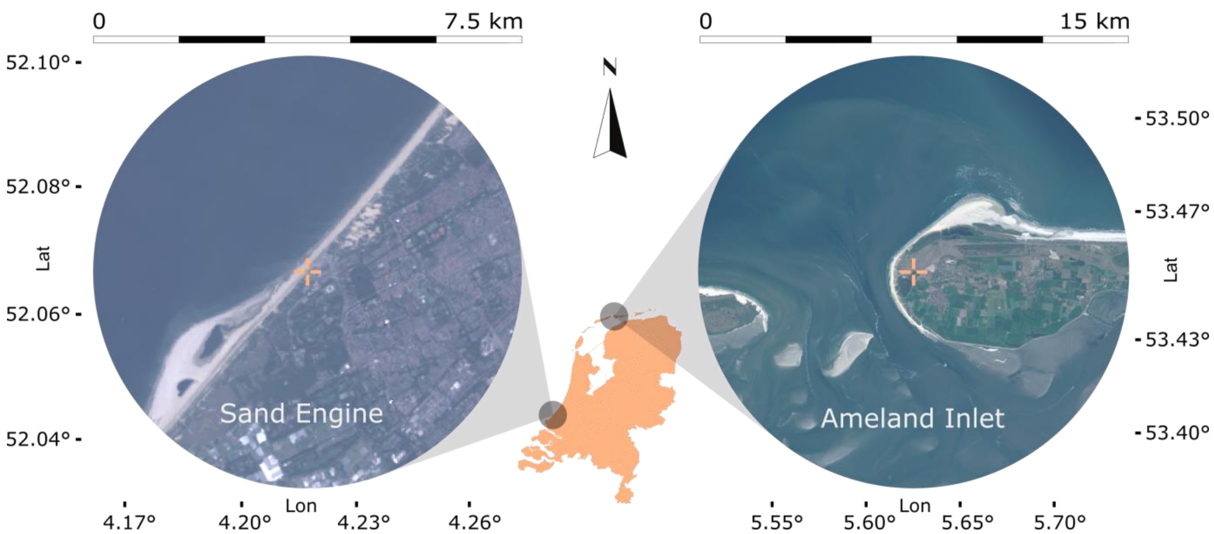

Figure 3. Radar locations (centre crosses) and ranges (see top scales) at the two field sites of Sand Engine (left) and the Ameland inlet (right). A map of the Netherlands (middle) indicates the location of the two sites.

3.1 Sand Engine

The first field site is the Sand Engine, a sandy mega-nourishment of approximately 21 Mm^3 constructed on the southwestern Dutch coast in 2011 (Figure 3,left). It was designed to combat erosion by diffusing along the coastline over an extended period of 10-20 years, while minimizing ecological stress and creating space for recreation (Stive et al., 2013). To gain insight into the development and impact of the unprecedented scale of the nourishment an extensive monitoring campaign was launched in 2012 (de Schipper et al., 2016). A radar station was installed 3 km north of the nourishment area, covering approximately 40 km^2. The available radar data covered a short timeframe of 18 h during 20-21 October 2014 and were used to create a snapshot of the nourishment for that moment. Specific details on the radar properties are summarized in table A.1.

The significant wave height (H_s) ranged from 1.0 m to 1.7 m and the peak period (T_p) from 6.0 s to 7.0 s, which are average wave conditions for the site (de Schipper et al., 2016). In total, 184 image sequences were available, each consisting of 128 images in intervals of 2.85 s, translating to 6 min of wave motion at a resolution of 3.75 m. Ground truth data were based on a detailed bathymetrical survey from 6 September 2014 which was merged with Jarkus transect data from 2014 to get greater coverage offshore. A local tide gauge was used to compensate for water level fluctuations in the depth estimates. For consistency, we only use the term depth throughout this paper, but note that it excludes the influence of water level modulation and is referenced to NAP (Dutch ordnance datum, about Mean Sea Level) for both sites.

3.2 Ameland tidal inlet

The second field site is the Ameland Inlet, one of the tidal inlets of the Dutch Wadden Sea (Figure 3,right). The inlet is characterized by a wave-dominated ebb-tidal delta and deep tide-dominated inlet channels formed by strong tidal currents with maximum velocities around 1.5 m/s. The semi-diurnal tide has a mean range of approximately 2 m. Over the study period Dec 2017 – Dec 2018, H_s ranged from 0.1 m to 6.2 m and T_p from 1.8 s to 17.0 s. Wave conditions were on average H_s = 1.3 m and T_p = 5.6 s and exceeded H_s > 3.0 m and T_p > 9.0 s during 5% of the time.

The inlet is being extensively monitored within the framework of the Coastal Genesis 2.0 (*Dutch*: Kustgenese 2.0) research program, which was commissioned by the Dutch Ministry of Infrastructure and Environment in 2017 (Van Prooijen et al., 2019). As part of the monitoring program, XMFit software runs operationally on X-Band radar data collected at the Ameland lighthouse. The navigational radar monitors the tidal inlet and has a spatial coverage of approximately 180 km^2 (Figure 3,right). Specific details on the radar properties can be found in table A.1. The goal of employing the radar is to track the evolution of a pilot nourishment of 5 million m^3 at the outer rim of an ebb-shield. Commencing 20 March 2018, the gradual placement of the nourishment ended in February 2019.

Radar image sequences at Ameland consist of 256 images spaced at 2.85 s. Image sequences cover a time window of 12 min and are produced at 20 min intervals, leaving 8 min of downtime in between. The pixel size is 7.5 m. Note that the range resolution is 7.5 m, but that the beam widens with distance from the radar. Depending on the alignment of the radar beam and wave crests, we estimate the resolution to be between 7.5 m and 57 m at 7 km distance from the radar (see also table A.1). Due to presently limited storage space (in this case 16 TB), raw image sequences (each 3 GB) are overwritten after 2 months and hence not available for reanalysis. The image sequences are processed locally in the light house such that the much smaller sized result files (each 0.1-0.5 MB) can be transferred via a 4G internet connection. Note that the storage buffer allows for the analysis of up to 72 image sequences a day; the increasing lag can be caught up during times when $H_s < 0.9$ m.

Poor depth estimates were supressed by tightening criterion (1) (section 2) using an averaging window of $M = 5$ and a depth margin of $\Delta d = 4$ m. Initial bathymetry data was needed to start the process. Tidal depth modulation was accounted for by passing information from a local wave buoy at Terschelling (Figure 1: grey square, top right). As initial bathymetry data a combination of surveys from February and September 2017 was used. Their initial influence on the estimates quickly phased out due to the choice of a rather large depth margin Δd. To additionally ensure that presented depth estimates were independent from the initial bathymetry the first 1000 estimates were ignored in this study. The choices for the averaging window and the allowable depth margin were made arbitrarily and other values may be chosen, yet the current combination of values underlies the results presented in this study.

Between Dec 2017- Dec 2018, the operational system returned approximately 7500 estimates of morphology. Within this period the Ameland Inlet was surveyed twice using a single beam mounted on a vessel. The first survey was done in the beginning stage of nourishment works 31 May – 5 June 2018 (Survey #1) and the second survey about half way, from 12 – 14 October 2018 (Survey #2). The surveys were done during calm periods that fell below the threshold of H_s = 0.9 m used by the operational system to produce depth estimates. For validation, therefore the average was taken over daily median estimates with similar spatial coverage shortly before and after each survey. Specifically for the nourishment location, additional multibeam surveys were available, which were used in this study to compute volumetric changes over the placement period of the nourishment.

The computational grids and user settings underlying the analyses of both the Sand Engine and the Ameland Inlet can be found in Appendix B.

4 Results

4.1 Sand Engine

The application of XMFit to radar images from the Sand Engine produced spatially smooth depth estimates (Figure 4a). Comparison of the median depth inversions with depth measurements revealed an overall bias of -0.9 m, revealing a tendency for depth overestimation by the DIA. The average standard deviation around a depth estimate was 0.85 m and likely stemmed from tidally induced changes in flow direction relative to the direction of wave incidence, see also Discussion section 5.1. The spatial root mean square error (RMSE) was 1.32 m and was mostly caused by inaccuracies close to shore and at the northern boundary of the radar domain. Near the shoreline, especially around the 5 m depth contour (Figure 4b), waves start to break over the nearshore bars and the used linear wave theory is not representative, which causes errors to be locally larger. This is similar to a previous observation by Bell, (2001) for Egmond aan Zee, a site about 60 km to the north of the Sand Engine. Close to the boundary of the radar domain, the radar image quality degrades. Furthermore, at the north-eastern end of the domain the radar beam aligns with wave crests, and depth estimates were poor or not returned. It is interesting to observe that estimates at large depths d = 10-15 m were generally close to ground truth, although peak wave periods were relatively short T_p = 6-7 s, meaning that an error in wavenumber leads to a large error in depth. There are two reasons why such errors are limited in the current approach: First, wavenumber errors are minimized through spectral averaging with 5 temporal bins (see Appendix B). Secondly, many spectral coordinates are used for the non-linear fit (Figure 1, ⑤). For the Sand Engine at these large depths on average about 75 coordinates spread over several angles and 11 frequencies. An important property of 3D-FFTs in combination with anti-aliasing is that frequencies up to two times the Nyquist frequency can be used for the fit (Seemann et al., 1997; Senet et al., 2001). This supplies extra spectral coordinates for the fit (red points above Nyquist frequency in Figure 2), which especially for T_p = 5-6 s can offer some extra certainty on the depth estimate in this case.

Note that it is possible to improve the results by making changes to the spectral treatment of the radar data or by using a Kalman filter in post-processing, which we address in the Discussion section 5.

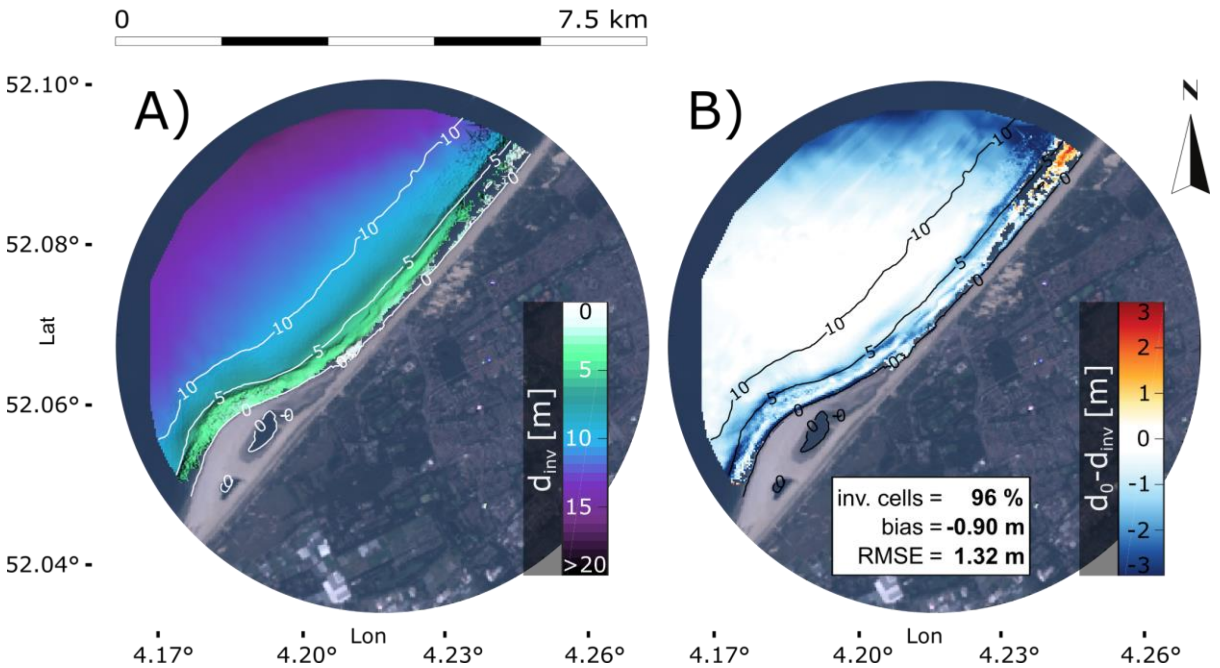

Figure 4. Radar-derived results for the Sand Engine. (a) Inverted depths d_{inv} (m) (colorbar). (b) Comparison of d_{inv} against in-situ measured depths d_0 (m), where red/blue colors indicate under-/overestimation of depth respectively. In both panels, contour lines of measured depths are superimposed for reference. Results represent the median over 184 image sequences spanning 18 h in total. Values are included for the percentage of grid cells returning a result (inv. cells), the overall bias (bias) and the root mean squared error (RMSE).

4.2 Ameland Inlet

Depth results for the Ameland Inlet distinctly captured the characteristic morphological features of the outer delta (Figure 5a,c). The horseshoe-shaped ebb-shield in the west, the central ebb channel, and the large swash platform fronting Ameland were detected by the algorithm. The estimated depths at instances of Survey #1 and Survey #2 compared to ground truth with spatially averaged biases of respectively 0.85 m and 0.63 m, and RMSEs of respectively 1.34 m and 1.14 m (Figure 5b,d), which were largely determined by inaccuracies between the 5-10 m contour lines. We hypothesize these imprecisions to be partly linked to complex local hydrodynamics, which are not accounted for by equation 1, in combination with some radar image related effects. For example, we expect some error due to tide driven shear flows in the channel between the ebb-shield and the swash platform and intense wave breaking and strong wave driven currents along the northern edges of these two features. In the region close to the island of Terschelling, in the western part of the domain (Figure 5b), we ascribe some error to the unfavourable angle of the radar beam with respect to the incoming wave crests. Yet another source of error was present, as the ebb-shield and the western branch of the ebb channel appeared slightly shifted to the south compared to single beam data. This shift stood out in the comparison with ground truth data (Figure 5b,d) through sharp negative biases around feature-edges facing north and corresponding positive biases around feature-edges facing south. Revisiting the raw radar images, revealed that this shift was partly rooted in a localized distortion of the raw radar image data, which was probably caused by a slight misalignment of the radars Northing, but the full origin is unknown and could therefore not be assessed in detail. In contrast, the system performed well for shallow parts such as the large swash platform near Ameland and deep parts to the north of the outer delta. Here, depth estimates were consistently accurate (Figure 5b,d: white areas).

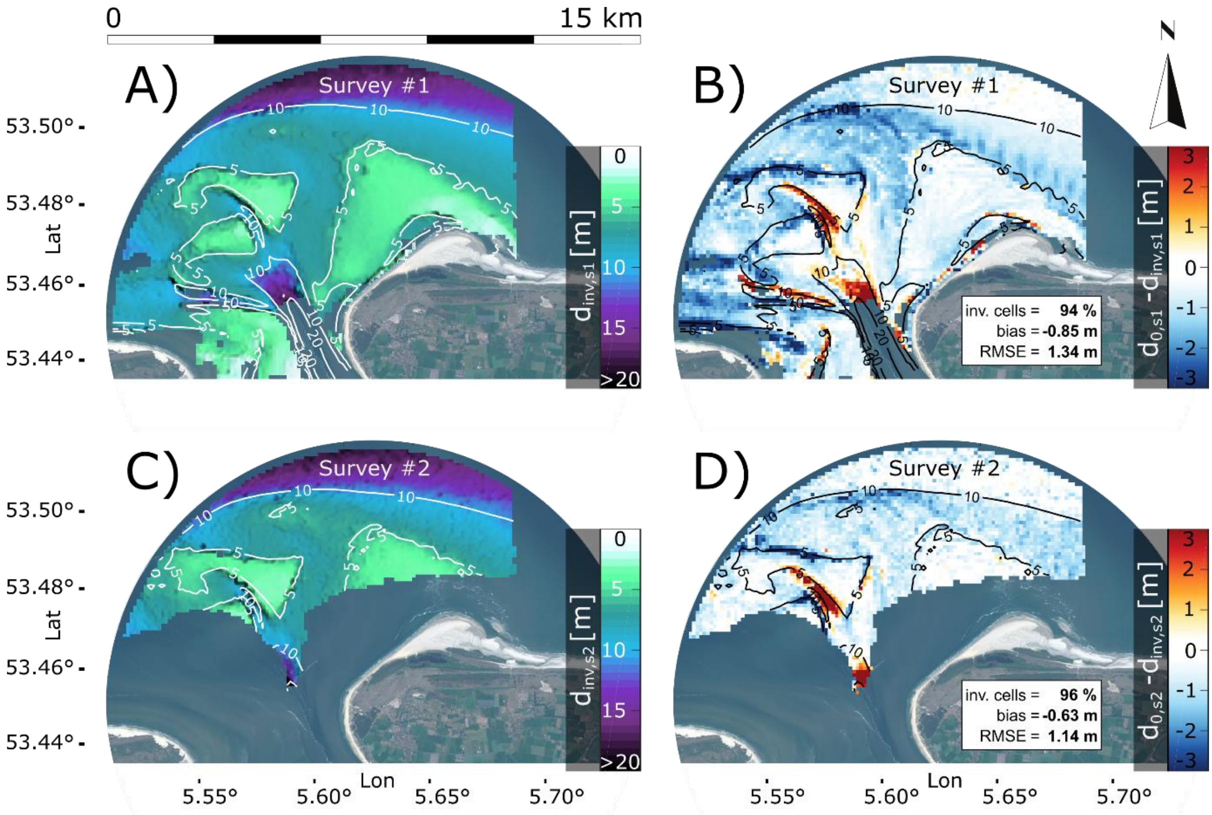

Figure 5. XMFit results from the operational Ameland system as compared to a survey from 31- May to 5- June 2018 (Survey #1) and a survey from 12-14 October 2018 (Survey #2). Panels (a,c): average depth estimates over two days encompassing each survey, as indicated by (a) $d_{inv,S1}$ for Survey #1 and (c) $d_{inv,S2}$ for Survey #2. Single beam observations are outlined by white depth contours. Panels (b,d): difference of inverted depths d_{inv} with the corresponding single beam measurements d_0 (now accentuated by black contours instead of white contours) as indicated by (b) $d_{0,S1} - d_{inv,S1}$ for Survey #1 and (d) $d_{0,S2} - d_{inv,S2}$ for Survey #2. Similar to the Sand Engine a mostly negative bias (depth overestimation; blue) is observed, being a little higher for Survey #1 (bias = -0.85 m) than Survey #2 (bias = -0.63 m).

The difference between the two time instances of Survey #1 and Survey #2 brought out the signature of the nourishment at the outer rim of the ebb-shield, in the single beam measurements (Figure 6b) as well as radar-inverted results (Figure 6a). These results were in line with the location of the nourishment site as provided by the dredging contractor. A succession of sedimentation-erosion patterns across north-eastern direction over the ebb-shield furthermore suggested a slight, clockwise turning of the ebb-shield over this four-month period. Although less pronounced than in the single beam measurements (Figure 6b), these patterns were also found in the radar-derived results (Figure 6a).

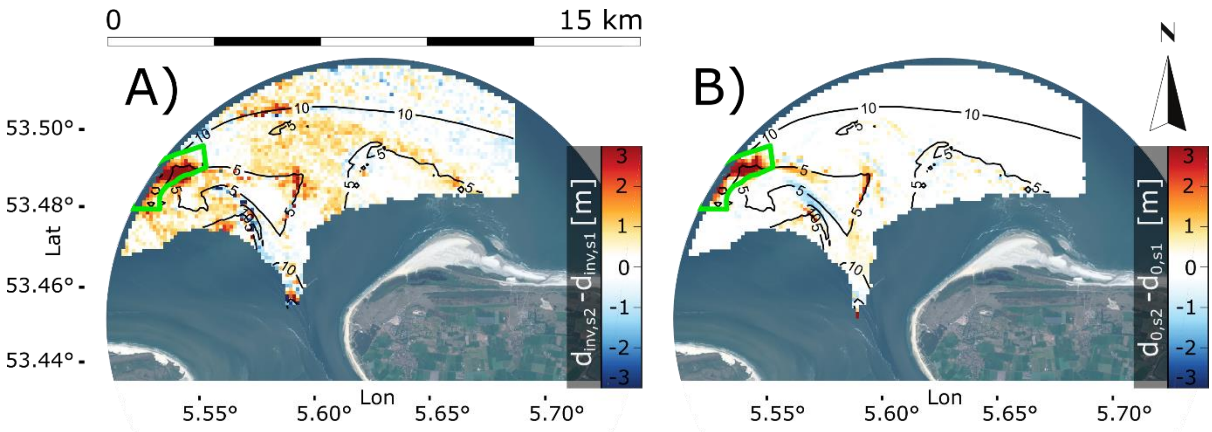

Figure 6. Difference between June (Survey #1) and October (Survey #2) as derived for radar and single beam measurements. (a) radar: inverted depths $d_{inv,S1}$, of Survey #1 are subtracted from $d_{inv,S2}$ of Survey #2. (b) single beam: accordingly, measurements $d_{0,S1}$ of Survey #1 are subtracted from $d_{0,S2}$ of Survey #2. The pilot nourishment fronting the ebb shield is clearly visible in both cases and its position is in line with expectation (green polygon). Note that the surveys do not cover the entire radar domain. For visual clarity, differences between radar results (a) are truncated to the same area as the surveys (b).

Since the nourishment was clearly visible in the time snapshots, the analysis was refined towards a more detailed time evolution to see whether we were able to monitor volume changes in the nourishment area during placement. For this, we used all the results produced between Dec 2017- Dec 2018. Before analysing nourishment volumes, the noise of the radar-derived depth estimates throughout the radar domain was assessed, as this noise could impact volume calculations. A timeseries of the spatially averaged depth bias was computed by the difference between radar-derived estimates and single beam data from Survey #1 (Figure 7). It was assumed that the influence of actual morphological change on the bias was negligible compared to the variability in radar depth estimations (cf. Figure 6b and Figure 5b). Although tidal water level changes were accounted for, the timeseries of depth biases fluctuated roughly between -2 m and 0 m. The average standard deviation around a daily depth estimate was 0.71 m. This noise was inherent to the operational system and was likely a product of a combination of factors, such as differences in radar image quality due to external factors (wind, rain, fog), but was also a consequence of applying idealized theory (equation 1) to a complex and variable outer delta environment: we found weak linear dependencies of the depth bias on the water level and the wind speed. For low water levels, NAP -1.5 m, the depth bias was on average -0.74 m and decreased linearly to -1.06 m for high water levels of NAP +1.5 m. Yet, with a standard deviation of 0.84 m the uncertainty in these depth bias values was high and showed that it would be difficult to predict the depth bias from a given water level. A similar linear relation was found between depth bias and wind magnitude: for wind speeds of 3 m/s the depth bias was on average ~ -0.5 m, while for wind speeds of 15 m/s this bias was ~ -1.2 m. Yet again, the standard deviation was high at 0.81 m, showing that a prediction of the depth bias based on wind speed would be uncertain. Depth estimates also correlated with simultaneous near-surface current estimates, whose directions and magnitudes are indicators for local depth underestimation or overestimation, as we discuss in detail in section 5.1. Since the current fields constantly change in space and time, they likely contribute to the observed fluctuations in the overall depth bias. No correlations of the depth bias with wind direction, wave height or wave period were found.

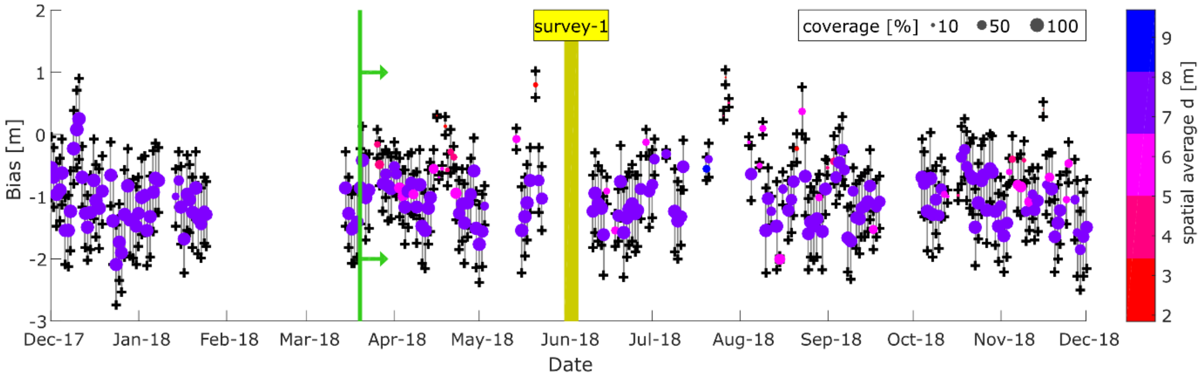

Figure 7. Mean spatial bias over the full radar domain of XMFit estimates with ground truth data surveyed between 31 May to 5 June 2018 (Survey #1, yellow). The start of nourishment works is indicated by a vertical green line. Representative bed elevations are obtained by subtracting local water level measurements from the XMFit depth estimates. Dots represent the daily median result and whiskers the corresponding 25^{th} and 75^{th} percentiles. Colors indicate the average depth over the parts of the radar image that contain results and show that the bias appears lower for moments when only small (small marker size), shallow (magenta, red) areas could be inverted. When coverage is high (large marker size) the bias also accounts for sensitive deeper parts (purple, blue). Note that the lack of data during February is due to a temporary system shutdown.

On the time scale of days, the observed noise would severely impact the calculation of nourishment volumes, therefore a straightforward solution was to ensemble average over a time window: we based volume calculations on median depth estimates in the nourishment area over a sliding time-window of one month. Besides denoising, volume estimates were then continuous in time, bridging over gap periods where the radar system had not been able to produce depth estimates for the nourishment area (Figure 8, gaps between grey bars). A window size of one-month was chosen as most data gaps could be overcome, except for a large gap in February 2018, while noise was largely suppressed. Volume changes were calculated by multiplying the average depth changes by the nourishment area (see Figure 6, green polygon). For the comparison, volumes were computed based on inverted depths as well as the depths from the multibeam surveys of the nourishment.

To focus the comparison between radar-estimates and multibeam measurements on volume changes, we referenced both the radar estimates and the measurements to the second multibeam measurement. The reason for this is a bias of 2 million m3 between the radar estimates and the measurements in the nourishment area at the time of the second multibeam survey (Figure 5). We assumed this bias to be constant in time, as fluctuations caused by environmental conditions and data quality should average out using a one-month averaging window over a long period of time. This meant that volume changes could be studied.

Computed volume changes in the nourishment area were relatively stable until they started to increase at the beginning of March 2018 (Figure 8). Considering the start of nourishment works (20. March 2018), this increase appeared two weeks premature. This could be explained by the one-month time window to suppress noise, while having no pre-nourishment data in February to counter balance March data. A RMSE of 276.000 m^3 was calculated based on the 7 instances where radar-derived volumes could be related to the multibeam surveys. It represented an error of 7% on the total placement volume of 3.8 million m^3. It is interesting to note that the location was at more than 7 km distance from the radar station, near maximum range.

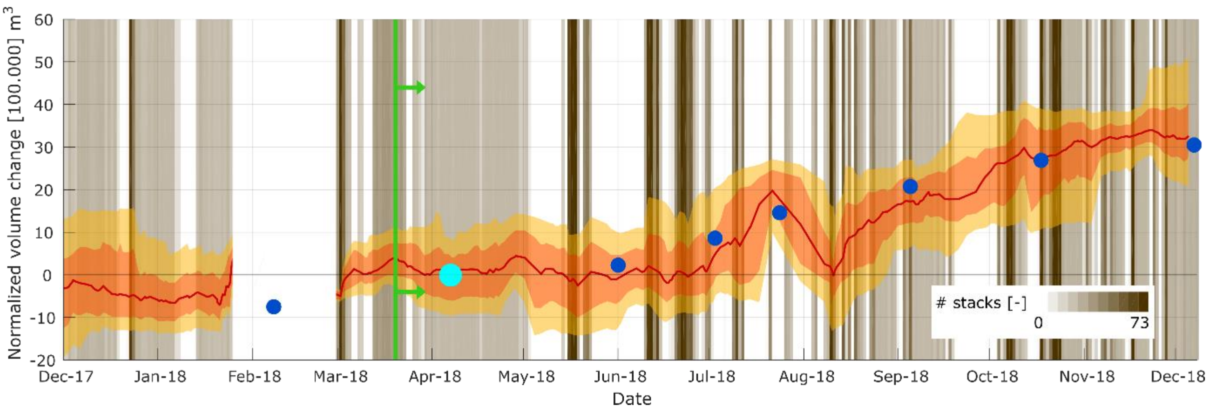

Figure 8. The time-evolution of the sediment volume changes in the nourishment area (Figure 6, green polygon) for the period Dec 2017 – Dec 2018 according to radar (red line) and multibeam surveys (blue dots). Volume changes are normalized to the 2nd multibeam survey (cyan dot). Per day, the number of available XMFit results that covered the nourishment area - and could hence be used for volume calculations - is indicated by a vertical grey band (see colorbar). The monthly median radar estimate (red line) is presented with corresponding 25 – 75 percentile range (shaded red) and 10th – 90th percentile range (shaded yellow). The start of nourishment execution, 20 Mar. 2018, is indicated by the vertical green line.

5 Discussion

The depth inversion showed skill for both the Sand Engine as well as the complex Ameland Inlet. Yet, the depth was often overestimated in regions (i) that were close to the boundary of the radar domain (ii) where the radar beam aligned with wave crests (iii) where we expected complex hydrodynamics due to wave breaking, strong currents or shear flows. These errors are related to the backscatter, but also to the limitations of using a simplified physical model (i.e., equation 1, idealized wave-current interaction) for depth inversion. The quality of d estimates by their covariance with $\boldsymbol{U}$ estimates provides insight into the role of the Doppler-shift. This is done from a statistical point of view, based on the extensive dataset from the Ameland Inlet (section 5.1). The d estimates can also be improved. By changing the computation procedure (section 5.2) and/or by post-processing the results (section 5.3), errors in (i) - (iii) are reduced. Experiments to reduce depth errors were conducted for the Sand Engine, since the image sequences could be recomputed at this site. Note that Ameland depth estimates were collected during a time where the DIA did not yet include a measure for error variance, which means that we could not test the Kalman filter on those data.

5.1 The role of near-surface current estimates in depth inversion

Near-surface currents are estimated per computational cube via the Doppler-shift ($+\boldsymbol{k}\cdot\boldsymbol{U}$, equation 1), being the dot product of a wavenumber vector with a near-surface current vector. Only current components in/against the wave direction alter the wave frequency and thereby affect the depth estimate d. To investigate the effect of $\boldsymbol{U}$ on d, near-surface current directions were translated to near-surface current angles (*NSCA*) with respect to wave direction, which was here taken to be the energy-weighted mean wave direction (*MWD*) over the spectrum.

First a preliminary check was done whether patterns of $\boldsymbol{U}$ and *MWD* were realistic and thereby suited for further analysis (Figure 9). This appeared to be the case: The *MWD* captured the effect of wave refraction, being stronger during low tide conditions (Figure 9c) than during high tide conditions (Figure 9a). It also revealed more intricate patterns as for example waves which followed ebb-channels to meet at the bifurcation just below the horseshoe-shaped ebb-shield (Figure 9c). Estimated $\boldsymbol{U}$-vectors also appeared realistic, reflecting the characteristic tidal flows expected for the area: The tidal wave travels along the barrier islands (Figure 9b,d: vector fields in north-northeast of domain) pushing water into the inlets at upcoming tide (Figure 9b: east-south-eastward flow through ebb-channels) and causing outward flow at falling tide (Figure 9d: westward flow through western ebb-channel and northward flow through central ebb-channel). Details such as flow through the small flood channels near Terschelling at rising tide were also captured.

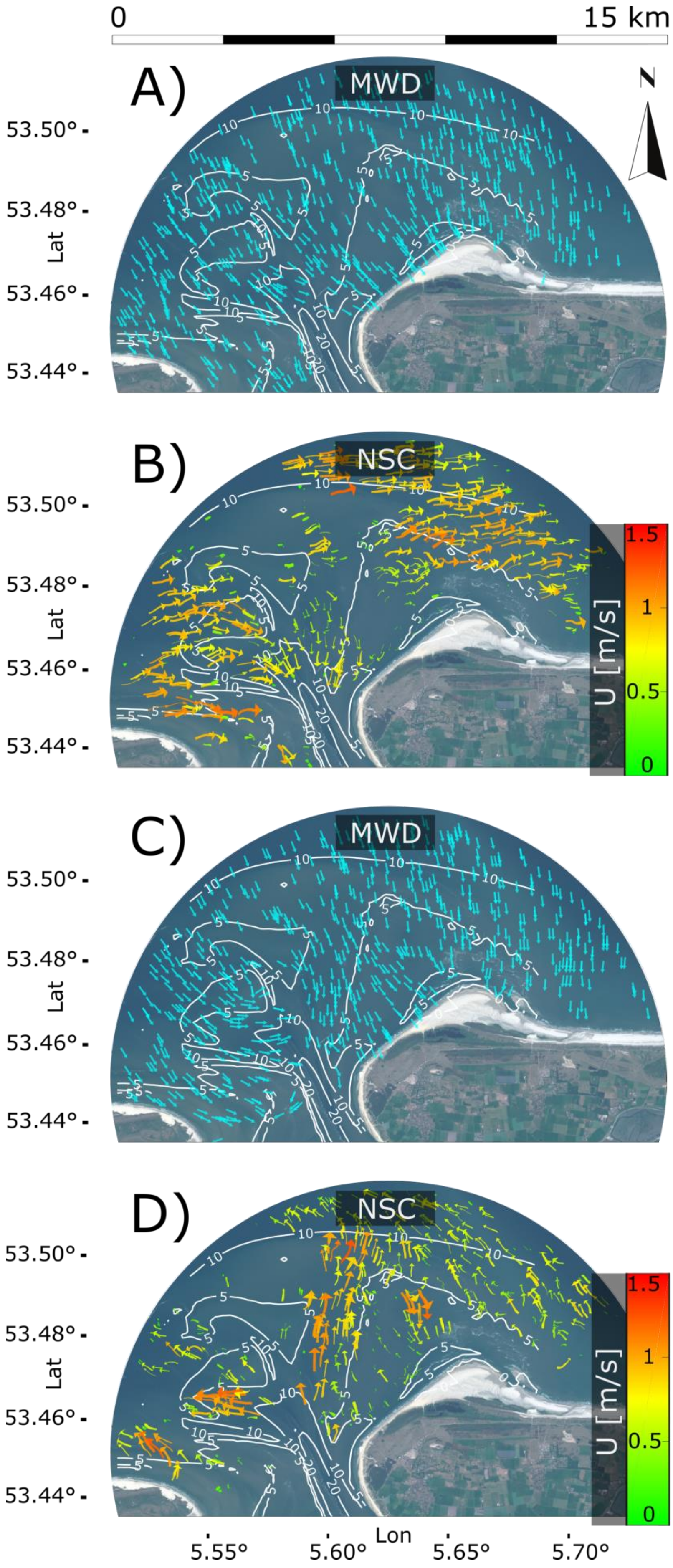
0
15 km
A)
MWD
B)
NSC
C)
MWD
D)
NSC
N
53.50°
53.48°
53.46°
53.44°
Lat
U [m/s]
1.5
1
0.5
0
Lon
5.55°
5.60°
5.65°
5.70°

Figure 9. Examples of mean wave directions (MWD) and near-surface currents (NSC) at the Ameland Inlet, as estimated by XMFit. Turquoise arrows indicate MWD-patterns. NSC arrows are scaled and colored according to magnitude (colorbar). Panels (a,b): An example from 25 Oct 2018 at 05:50, rising tide with a water level (WL) = NAP +1.1 m. Panels (c,d): An example from the preceding falling tide at 01:30, with WL = NAP -0.9 m.

For the Doppler-shift analysis, we retrieved the required *NSCA*s by expressing near-surface currents relative to the collocated *MWD*s. The accuracy of depth estimates was measured by the local depth bias $d_{0,S1} - d_{inv}$, which was computed for each cube in the domain and for all available time instances. In this way a comprehensive dataset was constructed, comprising more than 20 million pairs of depth biases and coincident near-surface current vectors. Analogous to Figure 7, we used Survey #1 as reference to calculate depth biases.

The analysis revealed that near-surface current estimates in direction of wave propagation ($NSCA \rightarrow 0°$) generally cooccurred with underestimation of depth, while near-surface current estimates against the direction of wave propagation ($NSCA \rightarrow \pm180°$) coincided with an overestimation of depth (Figure 10a: sinusoidal shape). These under- and overestimations increased with increasing near-surface current magnitudes (Figure 10a: bright colors at peak $NSCA = 0°$, and trough $NSCA = \pm180°$). However, weak near-surface current estimates in direction of wave propagation did not guarantee a good depth estimate (Figure 10a: dark colors between *NSCA* -60° to +63°). Still, the observations generally show that the Doppler-shift overcompensates for the presence of currents, as without the Doppler-shift we would expect current-induced depth errors to behave the opposite way (Honegger et al., 2020; eq. 10).

In shallow water, $d_{0,S1}$ = 0.5-5.0 m, depth overestimations and depth underestimations nearly balanced each other over the range of *NSCA*s from -180° to 180° (Figure 10b: median depth bias per *NSCA*, green curve, undulates around zero. Transition from general depth underestimation to overestimation at *NSCA* = ±73°, vertical magenta lines). This changed with increasing depth, $d_{0,S1}$ = 5.0-10.0 m, as depth overestimations started to dominate depth underestimations for most *NSCA*s (Figure 10c: green curve only positive for *NSCA* between -43° to +52°), with chronical overestimation for $d_{0,S1}$ = 10.0-25.0 m (Figure 10d: green curve stays below zero). However, in direction of wave propagation these overestimations were on average small with values close to zero (Figure 10d: green curve within *NSCA* < ± 90°). Besides the tendency towards depth overestimations, also the sensitivity in the depth estimates increased with increasing depth (cf. Figure 10b-d: bandwidth, given by 2.5th -97.5th percentile range, increases from b) ~3 m to c) ~4 m to d) ~6 m) especially for situations where near-surface current estimates pointed in direction of wave propagation (cf. Figure 10b-d: bandwidth larger for *NSCA* < ± 90°). It was interesting to observe that for shallow depths estimated maximum near-surface current magnitudes were larger in direction of wave propagation than against it (Figure 10b: brightest colors for *NSCA* $\rightarrow$ 0°, depth underestimation). For large depths, maximum near-surface current magnitudes were estimated against direction of wave propagation (Figure 10c,d: brightest colors for *NSCA* $\rightarrow$ 180°, depth overestimation), while near-surface current estimates in direction of wave propagation appeared to be underestimated (Figure 10c,d: dark colors for *NSCA* < ± 90°).

In summary, observed biases in both depth and near-surface current estimates suggest that the non-linear fit of equation 1 to the spectral data is sensitive to the local depth and the wave direction: (1) Generally, depths are underestimated for near-surface currents following the direction of wave propagation and depths are overestimated for opposing near-surface currents. (2) Strong near-surface current estimates correlate with strong depth biases, but a weak near-surface current estimate in direction of wave propagation does not guarantee a small depth bias. (3) For increasing depth, the depth estimate is more uncertain, tends towards overestimation, and especially so for opposing near-surface currents. (4) This is correlated with near-surface currents against direction of wave propagation having larger magnitudes than in direction of wave propagation.

The observations suggest that depth estimates may benefit from stricter constraints on maximum surface current magnitudes (e.g. $|\boldsymbol{U}_{max}| < 0.5$ m instead of $|\boldsymbol{U}_{max}| < 1.5$ m). This entails that it be difficult to find an optimal solution among the list of [d_i, $\boldsymbol{U}_i$]-candidates which satisfies the stricter criterion (Figure 1, 6). A way to solve this problem could be to penalize the non-linear fit for large $|\boldsymbol{U}|$.

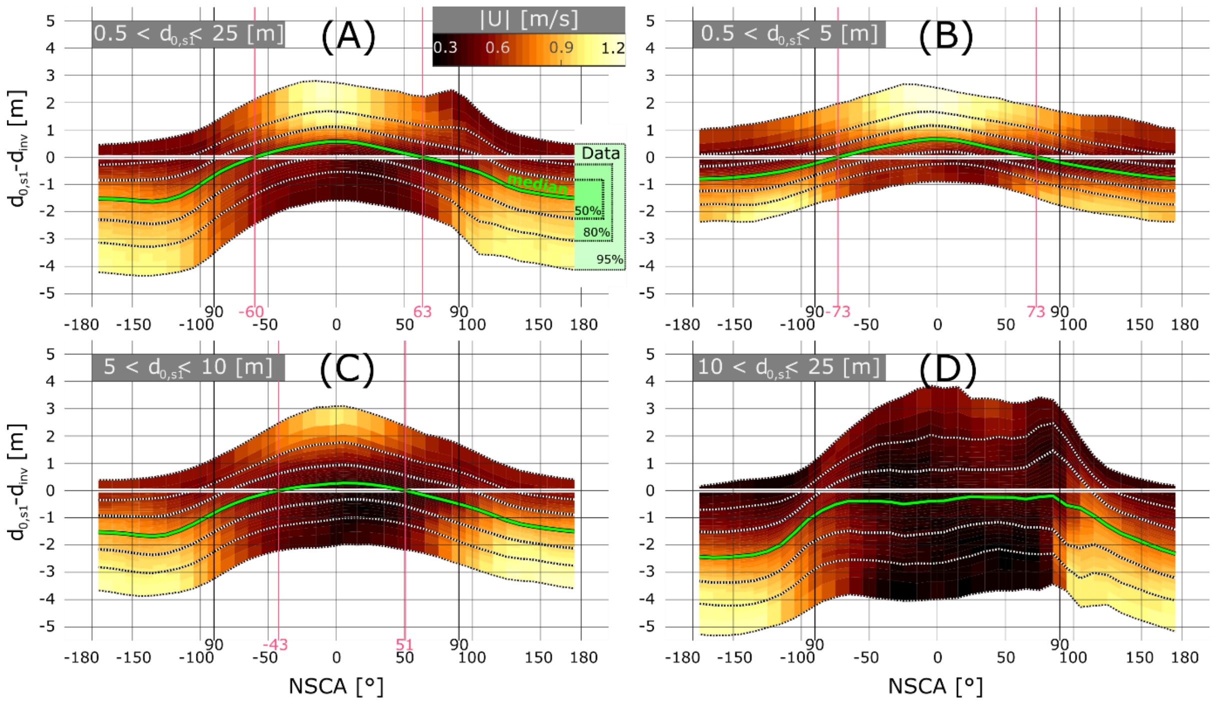

Figure 10. Observed depth bias (vertical axis) as a function of the near-surface current angle (*NSCA*) with respect to mean wave direction (horizontal axis). At *NSCA* = ±0°, near-surface currents point in direction of wave propagation, whereas for *NSCA* = ±180° they oppose each other. The depth bias is used as proxy for the depth error. Corresponding near-surface current magnitudes ($|U|$) are shown in bronze colors (colorbar). Panels present data within different ranges of depth: a) $0.5 < d_{0,s1} < 25.0$ m (all data); b) $0.5 < d_{0,s1} < 5.0$ m; c) $5.0 < d_{0,s1} < 10.0$ m;

d) 10.0 < $d_{0,s1}$ < 25.0 m. Depth biases are calculated as the difference between measured depths from Survey #1 and water level corrected inverted depths, $d_{0,S1} – d_{inv}$. Per *NSCA*, the 95% range of observed depth biases is presented (bandwidth) along with their median value (green line); the 95%, 80% and 50% range contours are indicated with dotted black lines and labelled as shown by the green boxes in panel (a). *NSCA* = ±90° are emphasized by additional vertical grid lines, to indicate where near-surface currents have no effect on waves according to equation 1. The angles that are optimal for depth inversion are given by the zero crossings of the median depth bias and are emphasized by vertical magenta grid lines. The dataset includes the results of all analysed cubes over the entire period from Dec 2017 – Dec 2018, amounting to > 20 million observations.

5.2 Choice of spectrum (amplitude vs. energy)

Depth estimates can also be improved in other ways. Depth inversion results are a product of relating wave characteristics to wave theory. A different representation of the wave characteristics may lead to different results, which is investigated by using amplitude spectra instead of energy spectra. The difference is simply that spectra are not squared after performing the 3D-FFT. It does not alter the wavenumber-frequency relationships, but their weights and hence changes the sets of spectral data that are passed to the non-linear fitter during the thresholding procedure (Figure 1, ⑤).

The results of this experiment suggest that more favorable sets of spectral data are established if amplitude spectra are used, as the overall depth bias (median over all analyzed image sequences) improved by 0.13 m, from -0.90 m to -0.77 m (cf. Figure 11a,b). The improvements especially occurred around the bars where waves break (Figure 11a,b, right column: red line vs. green line between d_0 = 4-8 m). This was also emphasized by an improvement of the bias by 0.22 m for the nearshore area, above the 10 m depth contour. Similarly, also the RMSE improved by 0.20 m from 1.32 m to 1.12 m with improvements being largest in shallow regions and the bar area. This effect can be explained by the disproportionate spectral weight of breaking waves in the image spectrum who by their asymmetry do not agree with the linear dispersion assumption underlying the analysis. Using an amplitude spectrum keeps the spectral weights closer together and thereby reduces the impact of breakers. Improvements were also noticed for the more difficult area to the north-east of the Sand Engine (Figure 11a,b,left column: whitening of north east area), which we ascribe to a relatively weaker impact of bad wave representations; in this case due to radar beam - wave crest alignment and lesser image quality.

5.3 Kalman filtering

An alternative way to improve the XMFit results is through post-processing with a Kalman filter. The Kalman filter is used in time on the derived morphological changes, assuming slowly varying morphology in comparison to the radar sampling interval, analogous to Holman et al. (2013). The Kalman filter is an instrument for quality control and improvement: It weighs the current depth estimate d_t at time t against a previous estimate $\bar{d}_{t-1}$ at $t-1$ using the Kalman gain, K, by $\bar{d}_t = \bar{d}_{t-1} + K(d_t - \bar{d}_{t-1})$, where overbars denote Kalman adjusted estimates. The Kalman gain requires an indication for the confidence we have in the current d_t estimate (R in eq. 5 of Holman et al. (2013)). In line with Holman et al. (2013), we use the error variance σ^2 of the non-linear fit for this purpose. This error variance of d_t is compared against the variance $\bar{\sigma}^2$ of $\bar{d}_{t-1}$ (P in eq. 5-7 of Holman et al. (2013)), which depends on previous estimates of σ^2, but also on process variance (Q in eq. 6 of Holman et al. (2013)). The process variance, Q, accounts for morphological change that may occur over the period of observations, but since Sand Engine data only cover a period of 18 h, we neglect it (i.e., $Q = 0$). For further details on the application of a Kalman filter to bathymetry estimates from a DIA, we refer to Holman et al. (2013). This experiment presents the results after the last, 184th Kalman filter iteration.

The Kalman filter reduced the depth bias by 0.21 m, from -0.90 m to -0.69 m, and the RMSE by 0.25 m, from 1.32 m to 1.07 m (cf. Figure 11a,c). In this case, the improvements were quite evenly distributed across all depths, including deeper areas (Figure 11a,c,left column: whitening of northern area; Figure 11a,c,right column: narrowing of d_{inv}-confidence interval for d_0 > 10 m). The combined effect of a Kalman filter and an analysis based on amplitude spectra was a reduction of the overall depth bias to -0.58 m and RMSE to 0.88 m (Figure 11d). The broad improvements clearly showed when compared to the base case (cf. Figure 11a,d): Depth estimates of the difficult regions in the north and north-east improved (Figure 11a,d,left column), but also the breaker region (Figure 11a,d,right column), which is known to experience larger errors (Bell, 2008). Hence, on the short term, the application of a Kalman filter without process variance is superior to using the median estimate. Though we recommend the data to cover at least one tidal cycle as to dampen out temporary tide induced inaccuracies.

Although we could not test the Kalman filter on the Ameland data, due to lacking information on σ^2, it is also not straightforward to apply. While the Kalman filter has proved itself valuable for the Sand Engine and also other uniform coastlines such as Duck (Holman et al., 2013), more complex coastal systems – like an ebb-tidal delta – may pose a problem when viewed over long periods of time, as morphological change needs to be described by process variance as a function of time and location, $Q(t,x,y)$. Tidal deltas are subject to various drivers and mechanisms that move sediment (Elias et al., 2019; Lenstra et al., 2019). Their influence and interactions continuously change in both space and time, which makes it difficult to formulate and quantify $Q(t,x,y)$. A spatiotemporally uniform implementation could be the choice of an upper bound $Q = max(morphological\ change)$, however, remains subject for further study.

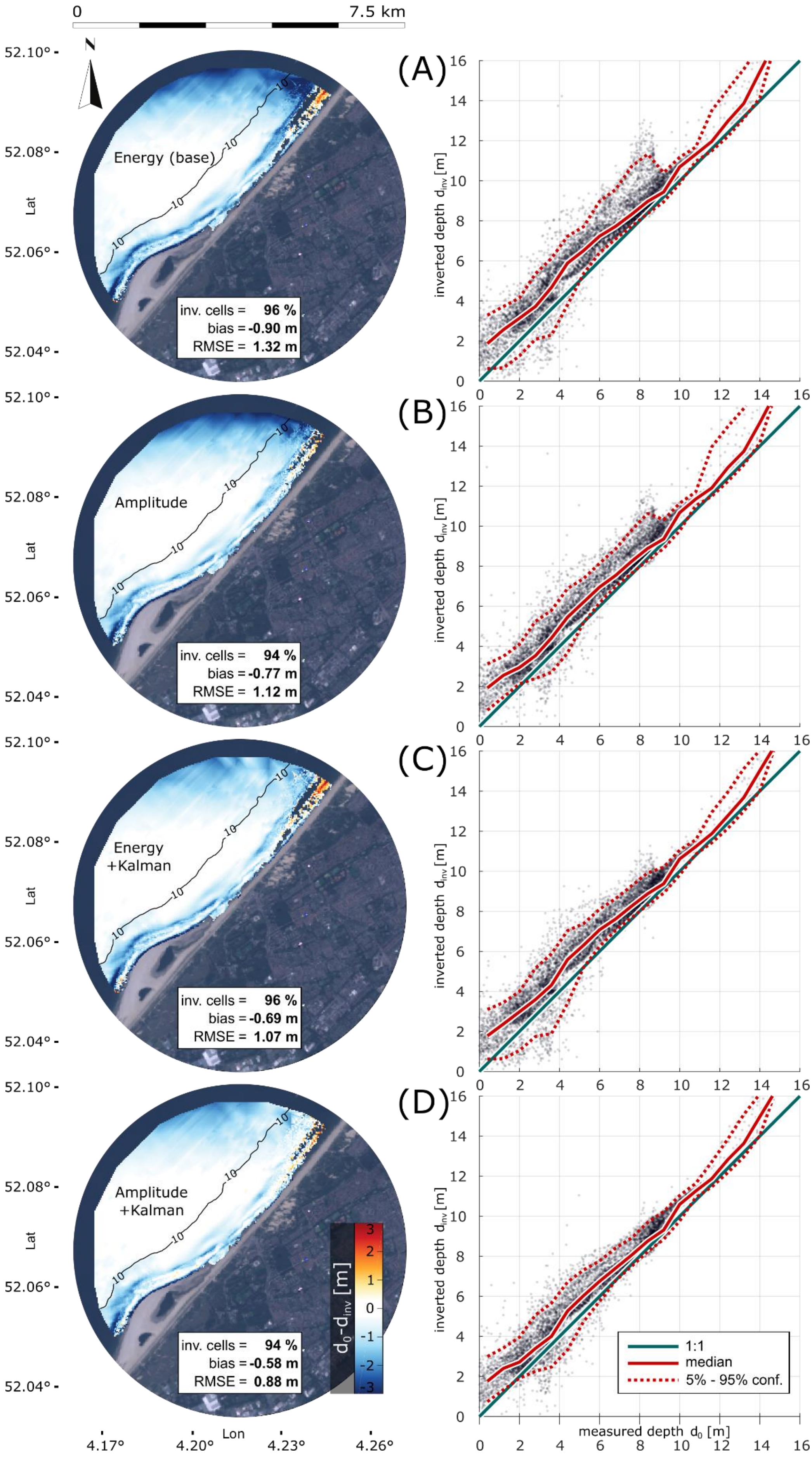
0
7.5 km
Energy (base)
inv. cells = 96 %
bias = -0.90 m
RMSE = 1.32 m
Amplitude
inv. cells = 94 %
bias = -0.77 m
RMSE = 1.12 m
Energy
+Kalman
inv. cells = 96 %
bias = -0.69 m
RMSE = 1.07 m
Amplitude
+Kalman
inv. cells = 94 %
bias = -0.58 m
RMSE = 0.88 m
Lat
Lon
(A)
(B)
(C)
(D)
inverted depth d_{inv} [m]
measured depth d_0 [m]
d_0-d_{inv} [m]
1:1
median
5% - 95% conf.

745

Figure 11. Methods to improve the XMFit results for the example case of the Sand Engine, shown by comparisons of inverted depths d_{inv} (m) against in-situ measured depths d_0 (m). The left column presents difference maps where red/blue colors indicate under-/overestimation of depth respectively. The right column presents direct comparisons of d_{inv} against d_0, including the 1:1 reference (green), the median over all d_{inv} at a certain d_0 (red), and the 5%-95% confidence interval (dashed red). Panels (a,b): Median depth estimates over all 184 image sequences from 20-21 Oct. 2014, for (a) the base case using the energy spectrum and (b) using the amplitude spectrum. Panels (c,d): The final, 184th estimate of the Kalman filter after application to results produced using (c) energy spectra and (d) amplitude spectra.

By reducing both bias and RMSE, the change of spectrum (section 5.2) and the Kalman filter (section 5.3) have demonstrated that results can be improved. Stricter constraints on near-surface current magnitudes may also increase the accuracy of depth estimates (section 5.1). Future work might provide insights that could lead to additional improvement of the results since some bias and RMSE remains. Early thoughts on common sources of error are (i) more radar image pre-processing to enhance radar image quality with increasing distance from the sensor, for example using FFT-accelerated video reconstruction techniques (Chan et al., 2011) (ii) the application of multiple radars to cover unfavourable wave-angles and (iii) including breaker intensity as a proxy for depth-induced dissipation to improve estimates in breaker zones (van Dongeren et al., 2008).

6 Conclusions

A depth inversion algorithm (DIA), XMFit (**X**-Band **M**ATLAB **Fit**ting), is a radar-based technique to monitor coastal evolution on large space (10s of kilometers) and time (months) scales. We mapped and analyzed two nourishments in the Netherlands using this technique: (1) an 18-hour snapshot of the beach mega nourishment, the Sand Engine, and (2) a one-year time-series of a 5 million m^3 pilot nourishment in the ebb-tidal delta of the Wadden Sea island Ameland. Derived morphologies in both cases largely agreed with ground truth data. Depth biases were around -0.9 m at Sand Engine and fluctuated between approximately -2 – 0 m at the Ameland ebb-tidal delta. By averaging and debiasing the radar-derived morphologies, it was possible to accurately quantify the growth of the ebb tidal delta nourishment at Ameland during its placement in 2018 with a volumetric margin error of 7%. Depth errors in the Ameland delta correlated with near-surface current magnitude and direction relative to the direction of wave propagation. The depth errors were generally smaller for small surface current magnitudes and respectively showed under- and overestimation for near-surface currents, in and against the direction of wave propagation. For the Sand Engine, experiments with the spectral treatment and the conceptual employment of a Kalman filter in post-processing improved the depth bias to 0.6 m. Further improving the results and the algorithm remains a scientific and operational challenge.

This research presents the successful operation of a DIA on data from a navigational X-Band radar to monitor a mega nourishment in a complex tidal inlet system, allowing coastal managers to assess volume changes over time.

Acknowledgements

This work was funded by the Dutch Ministry of Infrastructure and Environment through the Coastal Genesis 2.0 (*Dutch*: Kustgenese 2.0) project (1220339-007); the Deltares Strategic Research programs “Quantifying Flood Hazards and Impacts” (11203750) and “Future-proof Coastal Infrastructure and Offshore Renewable Energy” (11203765); and the TU Delft COCOS-Lab project as part of the ZABAWAS research program. Special credit goes to Joshua Friedman who is the founder of XMFit and by that made this research possible. NORTEK provided invaluable support in the collection of radar data and by sharing knowledge on depth inversion techniques. Thanks to the CIV (Rijkswaterstaat Centrale Informatievoorziening) for offering the Ameland radar as a remote sensing platform. We also like to mention the great amount of freely accessible code provided by amongst others the Deltares Open Earth Community and the Technical University of Denmark (“immoptibox” toolbox).

REFERENCES

Aarninkhof, S.G.J., Ruessink, B.G., Roelvink, J.A., 2005. Nearshore subtidal bathymetry from time-exposure video images. J. Geophys. Res. Ocean. 110, 1–13. https://doi.org/10.1029/2004JC002791

Bell, P., 2008. Mapping Shallow Water Coastal Areas Using a Standard Marine X-Band Radar. Hydro8, Liverpool, 4th-6th Novemb. 2008 1–9.

Bell, P., 2001. Determination of bathymetry using marine radar images of waves. Ocean Wave Meas. Anal. 251–257. https://doi.org/10.1061/40604(273)26

Bell, P., 1999. Shallow water bathymetry derived from an analysis of X-band marine radar images of waves. Coast. Eng. 37, 513–527. https://doi.org/10.1016/S0378-3839(99)00041-1

Bergsma, E.W.J., Conley, D.C., Davidson, M.A., O'Hare, T.J., Almar, R., 2019. Storm event to seasonal evolution of nearshore bathymetry derived from shore-based video imagery. Remote Sens. 11, 1–23. https://doi.org/10.3390/rs11050519

Borge, J., Rodríguez, R., Hessner, K., González, P., 2004. Inversion of marine radar images for surface wave analysis. J. Atmos. Ocean. Technol. 21, 1291–1300. https://doi.org/10.1175/1520-0426(2004)021<1291:IOMRIF>2.0.CO;2

Campana, J., Terrill, E.J., de Paolo, T., 2016. The development of an inversion technique to extract vertical current profiles from X-band radar observations. J. Atmos. Ocean. Technol. 33, 2015–2028. https://doi.org/10.1175/JTECH-D-15-0145.1

Chan, S.H., Khoshabeh, R., Gibson, K.B., Gill, P.E., Nguyen, T.Q., 2011. An augmented Lagrangian method for total variation video restoration. IEEE Trans. Image Process. 20, 3097–3111. https://doi.org/10.1109/TIP.2011.2158229

de Schipper, M.A., de Vries, S., Ruessink, G., de Zeeuw, R.C., Rutten, J., van Gelder-Maas, C., Stive, M.J.F., 2016. Initial spreading of a mega feeder nourishment: Observations of the Sand Engine pilot project. Coast. Eng. 111, 23–38. https://doi.org/10.1016/j.coastaleng.2015.10.011

de Vriend, H., van Koningsveld, M., 2012. Building with Nature: Thinking, acting and interacting differently., EcoShape, Building with Nature. https://doi.org/10.1080/02513625.2014.925714

Dugan, J.P., Piotrowski, C.C., Williams, J.Z., 2001. Water depth and surface current retrievals from airborne optical measurements of surface gravity wave dispersion. J. Geophys. Res. Ocean. 106, 16903–16915. https://doi.org/10.1029/2000jc000369

Elias, E.P.L., Van der Spek, A.J.F., Pearson, S.G., Cleveringa, J., 2019. Understanding sediment bypassing processes through analysis of high-frequency observations of Ameland Inlet, the Netherlands. Mar. Geol. 415, 1–27. https://doi.org/10.1016/j.margeo.2019.06.001

Flampouris, S., Seemann, J., Senet, C., Ziemer, F., 2011. The influence of the inverted sea wave theories on the derivation of coastal bathymetry. IEEE Geosci. Remote Sens. Lett. 8, 436–440. https://doi.org/10.1109/LGRS.2010.2082491

Hamm, L., Capobianco, M., Dette, H.H., Lechuga, A., Spanhoff, R., Stive, M.J.F., 2002. A summary of European experience with shore nourishment. Coast. Eng. https://doi.org/10.1016/S0378-3839(02)00127-8

Hessner, K., Reichert, K., Carlos, J., Borge, N., Stevens, C.L., Smith, M.J., 2014. High-resolution X-Band radar measurements of currents , bathymetry and sea state in highly inhomogeneous coastal areas. Ocean Dyn. 989–998. https://doi.org/10.1007/s10236-014-0724-7

Hessner, K., Reichert, K., Rosenthal, W., 1999. Mapping of sea bottom topography in shallow seas by using a nautical radar. 2nd Int. Symp. Oper. Remote Sens. 16–20.

Hessner, K., Wallbridge, S., Dolphin, T., 2015. Validation of areal wave and current measurements based on X-band radar. 2015 IEEE/OES 11th Curr. Waves Turbul. Meas. CWTM 2015 1–10. https://doi.org/10.1109/CWTM.2015.7098102

Holland, T.K., 2001. Application of the linear dispersion relation with respect to depth inversion and remotely sensed imagery. IEEE Trans. Geosci. Remote Sens. 39, 2060–2072. https://doi.org/10.1109/36.951097

Holman, R., Plant, N., Holland, T., 2013. CBathy: A robust algorithm for estimating nearshore bathymetry. J. Geophys. Res. Ocean. 118, 2595–2609. https://doi.org/10.1002/jgrc.20199

Honegger, D.A., Haller, M.C., Holman, R.A., 2019. High-resolution bathymetry estimates via X-band marine radar: 1. beaches. Coast. Eng. 149, 39–48. https://doi.org/10.1016/j.coastaleng.2019.03.003

Honegger, D.A., Haller, M.C., Holman, R.A., 2020. High-resolution bathymetry estimates via X-band marine radar: 2. Effects of currents at tidal inlets. Coast. Eng. 156. https://doi.org/10.1016/j.coastaleng.2019.103626

Huisman, B., Walstra, D.-J., Radermacher, M., de Schipper, M., Ruessink, G., 2019. Observations and Modelling of Shoreface Nourishment Behaviour. J. Mar. Sci. Eng. 7, 59. https://doi.org/10.3390/jmse7030059

Kroon, A., van Leeuwen, B., Walstra, D.-J., Gerard, L., 2016. Dealing with uncertainties in long-term predictions of a coastal nourishment. Coast. Manag. 9–18. https://doi.org/doi: 10.1680/cm.61149.009

Lenstra, K.J.H., Pluis, S.R.P.M., Ridderinkhof, W., Ruessink, G., van der Vegt, M., 2019. Cyclic channel-shoal dynamics at the Ameland inlet: the impact on waves, tides, and sediment transport. Ocean Dyn. 69, 409–425. https://doi.org/10.1007/s10236-019-01249-3

Lodder, Q.J., Sørensen, P., 2015. Comparing the morphological behaviour of Dutch-Danish shoreface nourishments. Coast. Manag. Chang. coast, Chang. Clim. Chang. minds.

Ludeno, G., Reale, F., Dentale, F., Carratelli, E.P., Natale, A., Soldovieri, F., Serafino, F., 2015. An X-band radar system for bathymetry and wave field analysis in a harbour area. Sensors (Switzerland) 15, 1691–1707. https://doi.org/10.3390/s150101691

Plant, W.J., 1990. Bragg Scattering of Electromagnetic Waves from the Air/Sea Interface, in: Surface Waves and Fluxes. Springer, Dordrecht, pp. 41–108. https://doi.org/10.1007/978-94-009-0627-3_2

Rutten, J., De Jong, S.M., Ruessink, G., 2017. Accuracy of Nearshore Bathymetry Inverted from X-Band Radar and Optical Video Data. IEEE Trans. Geosci. Remote Sens. 55, 1106–1116. https://doi.org/10.1109/TGRS.2016.2619481

Seemann, J., Ziemer, F., Senet, C.M., 1997. A method for computing calibrated ocean wave spectra from measurements with a nautical X-band radar 1148–1154. https://doi.org/10.1109/oceans.1997.624154

Senet, C.M., Seemann, J., Ziemer, F., 2001. The near-surface current velocity determined from image sequences of the sea surface. IEEE Trans. Geosci. Remote Sens. 39, 492–

505. https://doi.org/10.1109/36.911108

Serafino, F., Lugni, C., Soldovieri, F., 2010. A novel strategy for the surface current determination from marine X-Band radar data. IEEE Geosci. Remote Sens. Lett. 7, 231–235. https://doi.org/10.1109/LGRS.2009.2031878

Stive, M.J.F., de Schipper, M.A., Luijendijk, A.P., Aarninkhof, S.G.J., van Gelder-Maas, C., van Thiel de Vries, J.S.M., de Vries, S., Henriquez, M., Marx, S., Ranasinghe, R., 2013. A New Alternative to Saving Our Beaches from Sea-Level Rise: The Sand Engine. J. Coast. Res. 290, 1001–1008. https://doi.org/10.2112/jcoastres-d-13-00070.1

Trizna, D.B., 2001. Errors in Bathymetric Retrievals using Linear Dispersion In 3D FFT Analysis of Marine Radar Ocean Wave Imagery. IEEE Trans. Geosci. Remote Sens. 39, 2465–2469.

Valenzuela, G.R., 1978. Theories for the interaction of electromagnetic and oceanic waves - A review. Boundary-Layer Meteorol. 13, 61–85. https://doi.org/10.1007/BF00913863

van Dongeren, A., Plant, N., Cohen, A., Roelvink, D., Haller, M.C., Catalán, P., 2008. Beach Wizard: Nearshore bathymetry estimation through assimilation of model computations and remote observations. Coast. Eng. 55, 1016–1027. https://doi.org/10.1016/j.coastaleng.2008.04.011

Van Prooijen, B.C., Tissier, M.F.S., De Wit, F.P., Pearson, S.G., Brakenhoff, L.B., Van Maarseveen, M.C.G., Van der Vegt, M., Mol, J.W., Kok, F., Holzhauer, H., Borsje, W., van der Werf, J., Vermaas, T., Gawehn, M., Grasmeijer, B., Elias, E., Tonnon, P.K., Reniers, A.J.H.M., Wang, Z.B., den Heijer, K., van Gelder-Maas, C., Wilmink, R.J.A., Schipper, C., de Looff, H., 2019. Measurements of Hydrodynamics, Sediment and Benthos on Ameland Ebb-Tidal Delta. Earth Syst. Sci. Data 1–18.

Young, I.R., Rosenthal, W., Ziemer, F., 1985. A three-dimensional analysis of marine radar images for the determination of ocean wave directionality and surface currents. J. Geophys. Res. 90, 1049–1059. https://doi.org/10.1029/JC090iC01p01049

Appendices

A

Table A.1. Radar properties at the Sand Engine and Ameland

Properties	**Sand Motor**	**Ameland Inlet**
Antenna Height [m, NAP]	15	60
System Type	Terma Scanter 2000	Terma Scanter 2001
Antenna Width [ft]	14	21
Range [km]	3.75	7.5
Pulse Length [ns]	50	60
Horizontal Beam Width [deg]	0.5	0.43
Vertical Beam Width [deg]	23	23
PRF [kHz]	4	2.2
Rotation Speed [rpm]	25	21
Output Power [kW]	25	25
Polarization	VV	VV

B

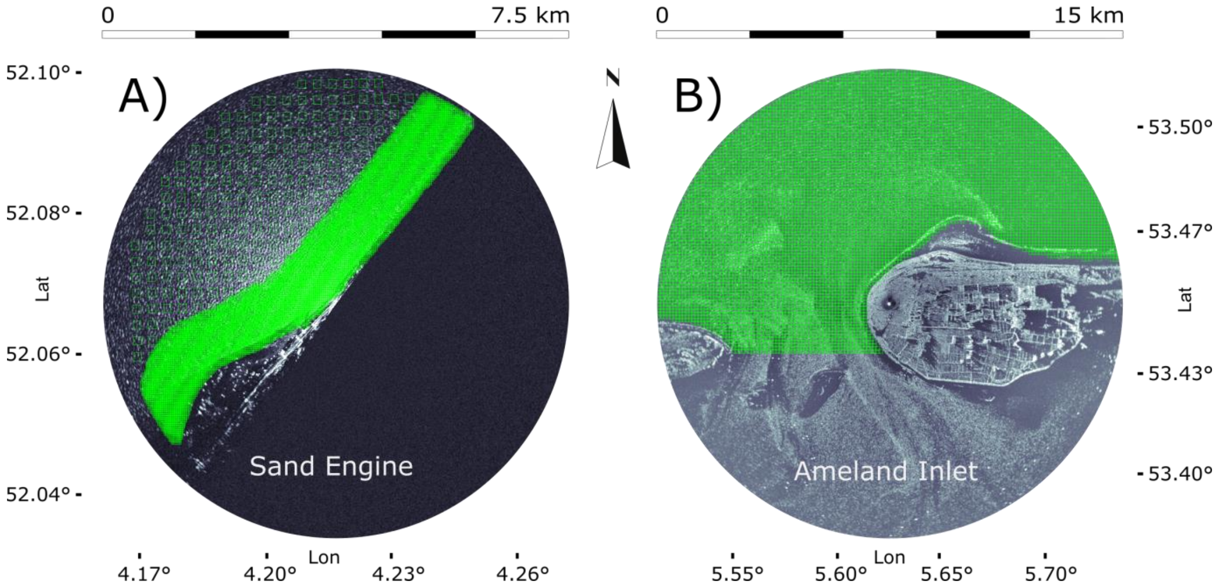

Figure B.1. Computational grids (green) used for (a) the Sand Engine (b) and the Ameland Inlet. The grids are overlaid on typical radar images of both sites.

Sand Engine

For computational efficiency of XMFit, a variable grid spacing of 25 m near the shoreline and 250 m further offshore was used, resulting in 9380 grid points. The computational cubes were time-averaged by subdividing them into 32 image bins with 8 images overlap. The spatial extents were 64px (240 m) within 300 m from the shoreline and 128px (480 m) further offshore. The reduced cube size in the nearshore region was chosen in order to capture more morphological detail.

For consistency, XMFit settings were chosen to be similar to the application at Ameland. The spectral frequency filter was set to include shorter wave periods, [T_{min}, T_{max}] = [3.5, 15] (s) (Figure 1, ②). Depth limits were set to [d_{min}, d_{max}] = [0.5, 25] (m) (Figure 1, ③), and the near-surface current velocity limit was set to $|\boldsymbol{U}_{max}|$ = 1.25 (m/s) (Figure 1, ⑥).

Ameland Inlet

In case of the Ameland Inlet, a constant grid spacing of 100 m was used amounting to 8328 grid points in total. Computational cubes were time-averaged using 32 image bins without overlap and had a spatial extent of 128px (960 m).

The inversion process was constrained by the wave period limits [T_{min}, T_{max}] = [5, 15] (s) (Figure 1, ②), depth limits [d_{min}, d_{max}] = [0.2, 25] (m) (Figure 1, ③), and $|\boldsymbol{U}_{max}| < 1.5$ (m/s) (Figure 1, ⑥).